


Spin-polarized Majorana zero modes in double zigzag honeycomb nanoribbonsR. C. Bento Ribeiro ^{1,2}, J. H. Correa ³, L. S. Ricco ⁴, A. C. Seridonio ⁵ and M. S. Figueira ^{1,*}¹*Instituto de Física, Universidade Federal Fluminense, Avenida Litorânea s/N, 24210-340, Niterói, Rio de Janeiro, Brazil*²*Centro Brasileiro de Pesquisas Físicas, Rua Dr. Xavier Sigaud, 150, 22290-180, Urca, Rio de Janeiro, Rio de Janeiro, Brazil*³*Universidad Tecnológica del Perú, Nathalio Sánchez, 125, 15046, Lima, Perú*⁴*Science Institute, University of Iceland, Dunhagi-3, IS-107, Reykjavik, Iceland*⁵*São Paulo State University (Unesp), School of Engineering, Department of Physics and Chemistry, 15385-000, Ilha Solteira, São Paulo, Brazil* (Received 19 August 2021; revised 2 February 2022; accepted 27 April 2022; published 12 May 2022)

We study the emergence of Majorana zero modes (MZMs) at the ends of a finite double zigzag honeycomb nanoribbon (zHNR), considering a minimal model composed of the first nearest neighbor hopping term, Rashba spin-orbit coupling (RSOC), p -wave superconducting pairing, and an applied external magnetic field (EMF). The energy spectrum profiles reveal regions with either spin up or down MZMs belonging to distinct topological phase transitions, which are characterized by their corresponding winding numbers and can be accessed by tuning the chemical potential of the nanoribbons. Hybrid systems constituted by zHNRs deposited on conventional s -wave superconductors are potential candidates for experimentally realizing our proposal. The spin discrimination of MZMs suggests a possible route for performing topological-conventional qubit operations using Majorana spintronics.

DOI: [10.1103/PhysRevB.105.205115](https://doi.org/10.1103/PhysRevB.105.205115)**I. INTRODUCTION**

Starting from the seminal work of Read and Green [1] on two-dimensional p -wave superconductors, Kitaev proposed a simplified one-dimensional (1D) toy model [2]. In this model, unpaired Majorana zero modes (MZMs) appear at opposite ends of a p -wave superconducting tight-binding chain. Remarkably, it took less than a decade [3] to understand that Kitaev's original proposal could be experimentally realized. Some setups [4–6] employed hybrid devices composed of a 1D semiconductor nanowire with strong Rashba spin-orbit coupling (RSOC), in contact with a conventional s -wave superconductor and under an external magnetic field (EMF) longitudinal to the nanowire. Topological protected MZMs emerge at the nanowire ends [7] when the nanowire chemical potential lies on the bulk p -wave superconducting induced gap.

Another kind of setup came up after the development of epitaxially grown hybrid semiconductor-superconductor systems in which two or three facets of the hexagonal InAs nanowire core were covered by Al [8]. This setup is a hybrid platform that employs a naturally occurring quantum dot (QD) at the end of the nanowire as a spectrometer [9–12] to measure the nonlocality degree and the spin canting angles of the nonlocal MZMs [13,14]. A chain of ferromagnetic atoms aligned over a conventional s -wave superconductor with strong RSOC also was considered as a hybrid system supporting the existence of MZMs [15,16]. In this scenario, the essential ingredients to generate MZMs at the ends of the chain are the ferromagnetic interaction between atoms

that compose the chain and the RSOC induced on the chain by the superconducting substrate. A helpful review of the experimental state of the art on this subject can be found in Refs. [17,18].

The manifestation of MZMs in 1D hybrid semiconductor-superconductor nanowires, known as Majorana nanowires, and magnetic chains on top of s -wave superconductors are fully understood from a theoretical point of view [7,19,20]. Recent works have been pointing out the need to fabricate cleaner and disorder-free Majorana nanowires with an induced hard superconducting gap [21–23], in which distinct measurements have to be performed to corroborate the existence of topologically protected MZMs [24–26]. In this scenario, alternative 2D honeycomb lattice setups offer a prolific and little-explored platform wherein topological Majorana quasiparticle excitations can emerge. Between them, we can indicate two theoretical precursor works: One proposes the generation of MZMs on quantum wires formed in bilayer graphene by electrostatic confinement [27] and the other studied the formation of MZMs on an armchair nanoribbon in the presence of spatially varying magnetic fields [28]. Both systems are put in contact with an s superconductor.

We also draw attention to zigzag honeycomb nanoribbons (zHNRs) built up from Xenes graphene-like family [29–31], where X represents single elements from group III to group VI of the periodic table. Despite the challenges of growing zHNRs of the Xenes family in conventional s -wave superconductors [32–34], such kinds of 2D lattice offer an alternative for engineering the p -wave superconducting pairing required to realize MZMs. Probably, silicene ($X = \text{Si}$) is the most promising candidate of this family for obtaining a zHNR geometry with the ability to host MZMs [35,36]. Its energy

*Corresponding author: figueira7255@gmail.com

spectra [37] can be spin polarized by applying an external electric field perpendicular to the zHNR sheet plane [38–40], giving rise to an effective extrinsic RSOC that breaks its mirror symmetry [see Eq. (7)]. Silicene also presents an excellent potential to produce half-metallic transport and pure spin current [41–43].

Another possibility discussed in Sec. IV to realize p -wave superconductivity to produce a Kitaev chain is related to the property of zHNRs from Xenes materials to exhibit ferromagnetic ordering at their edges [44] due to internal repulsive Coulombic interactions [31]. Thus, this inborn spin alignment at the zHNR edges can be employed to induce the superconducting pairing with p -wave symmetry when the zHNRs are put in proximity with a s -wave superconductor. This procedure is similar to previous works with ferromagnetic chains from Yazdani’s group [15,16], but we do not theoretically implement it in this paper.

Despite the spinless nature of Kitaev’s work, some proposals have explored the spin properties of MZMs in different contexts. Jeon *et al.* [16], employed a spin-polarized STM for distinguishing between topological MZMs and other trivial in-gap states in chains of Fe atoms deposited on top of superconducting Pb. Spin polarization of MZMs was also accounted for to investigate the Kondo effect in a QD coupled to a metallic contact and a pair of MZMs [45] and to study the transport properties of a finite-length Majorana nanowire placed between a dot and a metallic lead [14,46].

Since the theoretical work by Fu and Kane that MZMs was predicted to be present inside a core of vortex topological superconductors [47], the possibility of spin polarizing them was pointed out in Ref. [48]. Its experimental detection was realized in a topological insulator-superconductor $\text{Bi}_2\text{Te}_3/\text{NbSe}_2$ heterostructure [49]. The spin polarization of those core states can be probed by measuring the local polarized density of states (LDOS) employing scanning tunneling microscopy and spectroscopy (STM/STS) via excitations in the vortex state [50,51]. Moreover, the MZMs was also employed as an alternative way of performing quantum computing operations [52–54], allowing the transference of spin qubits QDs and unpolarized MZMs, and also realizing nontrivial two-qubit gates. As proposed in this work, the discrimination of the spin degrees of freedom of the MZMs in topological superconductor vortices or zigzag nanoribbons can contribute to building topological quantum gates employing the spins of both MZMs and QDs simultaneously.

In this work, we report the possibility of spin discriminating MZMs in zHNRs geometry [Fig. 1(a)], which we refer to as double-spin Kitaev zigzag honeycomb nanoribbons (KzHNR). This double nanoribbon structure mimics two parallel Kitaev chains connected by the hopping t , as indicated in Fig. 1(c). Our findings reveal that we can access the spin species of the MZMs in a double-spin KzHNR by tuning the chemical potential of the chains, which is not feasible in standard 1D Majorana nanowires. In this scenario, we suggest an experimental proposal to discriminate spin-polarized MZMs in zHNRs structures of silicene grown over a Pb superconductor in the presence of RSOC and an EMF. Our findings could contribute to paving the way for studying hybrid topological-conventional polarized QD qubits using Majorana spintronics.

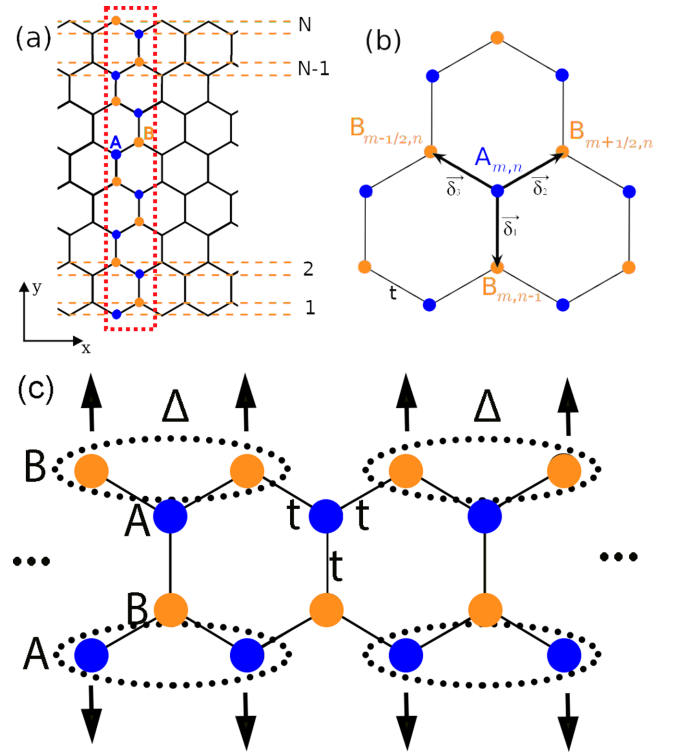


FIG. 1. (a) Sketch of the 2D zHNR geometry adopted here, where N represents its width ($n = 1, \dots, N$). The region within the red dashed area composed of $2N$ nonequivalent A (blue) and B (orange) sites along the y direction represents the unit cell employed in the numerical simulations. The M number of unit cells defines the nanoribbon length ($m = 1, \dots, M$). (b) Representation of the nearest neighbor hopping t , which is adopted as the energy unit. (c) Schematic of a double-spin KzHNR of width $N = 2$. The equivalent B (A) atoms of the upper (lower) KzHNR are paired with each other via a p -wave superconducting parameter Δ .

II. SPINLESS MODEL AND TOPOLOGICAL PHASE TRANSITIONS

We first consider a double-spinless KzHNR as a generalization of the Kitaev chain [2] to characterize the topological phase transitions (TPT) of the system through corresponding winding numbers [55], computed for the infinite case (more details in Appendix A). By considering a tight-binding chain in a zHNR geometry, we define a spinless phenomenological model as a Kitaev ladder type [56]. We represent in Fig. 1(c), the first nearest neighbor (NN) hopping t between nonequivalent sites A and B and the p -wave superconducting pairing, indicated by arrows, between equivalent sites A or B located at the edges of the KzHNR. The Hamiltonian describing such a model reads

$$H = H_t + H_\Delta, \quad (1)$$

where

$$H_t = \sum_{m,n} [t(a_{m,n}^\dagger b_{m,n-1} + a_{m,n}^\dagger b_{m-1/2,n} + a_{m,n}^\dagger b_{m+1/2,n}) - \sum_n \mu [a_{n,n}^\dagger a_{n,n} + b_{n,n}^\dagger b_{n,n}] + \text{H.c.}], \quad (2)$$

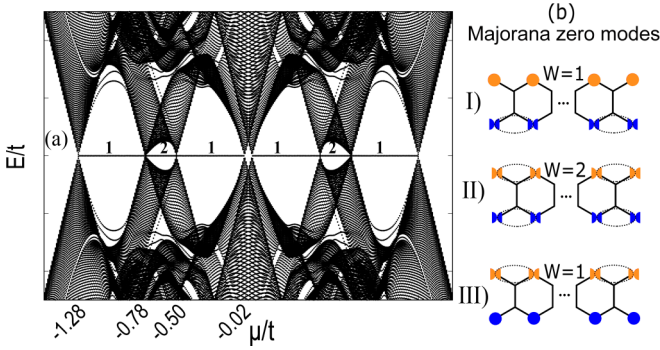


FIG. 2. (a) Energy spectrum of a 2D double-spinless KzHNR [Eq. (1)] as a function of μ and p -wave pairing $\Delta = 0.5t$, for a KzHNR of width $N = 2$ and length $M = 200$. The numbers on the real axis represent the W associated with the corresponding topological region. (b) Schematic representation of the emergence of MZMs at the ends of the KzHNR for each associated W . Each semicircle represents an MZM generated on the site of the active border of the KzHNR. The two Majoranas connected with the dotted ellipses form a standard fermion. In the topological phase, unpaired Majorana fermions emerge at both ends of each KzHNR, as represented by the semicircles outside the dotted ellipses. The situations (I) and (III) describe $W = 1$, where only the top or bottom KzHNR generates one MZM at each of its ends. Otherwise, in (II) $W = 2$, indicating that both the KzHNRs generate MZMs simultaneously at their corresponding ends.

corresponds to the NN hopping term t , as indicated in Fig. 1(b), where μ is the chemical potential and the operators $a_{m,n}^\dagger$ (or $b_{m,n}$) creates (annihilates) an electron at site A (B) of the unit cell. Moreover, the Hamiltonian

$$H_\Delta = \sum_{m,n} \Delta [a_{m,n}^\dagger a_{m+1,n}^\dagger - a_{m,n}^\dagger a_{m-1,n}^\dagger + b_{m,n+1}^\dagger b_{m+1,n+1}^\dagger - b_{m,n+1}^\dagger b_{m-1,n+1}^\dagger + \text{H.c.}] \quad (3)$$

describes the p -wave superconducting pairing of the double-spinless KzHNR, where Δ is the pairing strength between sites B in the top and between sites A in the bottom of each KzHNR, as indicated in Fig. 1(c). Once particle-hole, time-reversal, and chiral symmetries are preserved by the Hamiltonian [Eqs. (1)–(3)], it belongs to the BDI symmetry group class with \mathbb{Z} index [57,58] (see Appendix A). For simplicity, we only have considered a double-spinless KzHNR of width $N = 2$ in our numerical simulations. However, the results presented here are also valid for nanoribbons of larger widths.

Figure 2(a) shows the bulk energy spectrum E/t of the double-spinless KzHNR [Eq. (1)] as a function of the chemical potential μ/t . Several TPTs characterized by the closing and reopening of superconducting-induced gap appear at the $\mu = -1.28t$, $-0.78t$, $-0.50t$, and $-0.02t$, respectively. According to the bulk-boundary correspondence principle [59], the multiplicities of modes on the boundaries associated with the TPTs in bulk are characterized by topological invariants of the bulk energy bands, as the so-called winding number W , for instance. Here, we have found $W = 0$, $W = 1$ and $W = 2$ [see Figs. 6(a)–6(d)], which are indicated in the corresponding regions of Fig. 2(a). Following the bulk-boundary

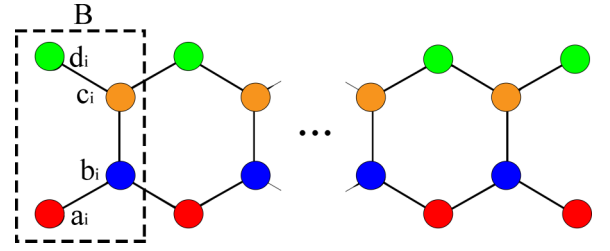


FIG. 3. Scheme of the basis adopted in the Hamiltonian given by the Eqs. (4)–(8) describing the finite double-spin KzHNR chain of width $N = 2$. The unit cell B , represented by the dashed rectangular area is built with four distinct atoms a_i , b_i , c_i , and d_i .

principle, $W = 0$ ($\mu > |1.28t|$) characterizes the trivial phase, where MZMs are absent at the ends of both the KzHNRs. Between $\mu = -1.28t$ and $\mu = -0.78t$, a topological region is characterized by $W = 1$, indicating the emergence of MZMs at opposite ends of either bottom or top KzHNR [Fig. 2(b), cases (I) and (III)].

Figure 2(a) also exhibits another topological region characterized by $W = 2$ in the interval $-0.78t < \mu < -0.50t$, for instance, corresponding to the situation in which the MZMs arises simultaneously in the ends of both top and bottom KzHNR, as indicated in the sketch (II) of Fig. 2(b). In Fig. 2(a), we also can notice that the same TPTs which occur for $\mu < 0$ appear for positive values of μ due to the particle-hole symmetry exhibited by the Hamiltonian of Eq. (1) [60].

III. SPIN FULL MODEL AND EMERGENCE OF SPIN-POLARIZED MZMS

To analyze the possibility of distinguishing the spin species of the MZMs, we now discuss the emergence of MZMs at the double-spin KzHNR geometry edges, considering both spin orientations explicitly. We account for the infinite version of the whole spin case in Appendix A [see Figs. 6(e)–6(k)]. Here we discuss the finite version of the model. To properly break the spin degeneracy of the system, we introduce two additional effects in the Hamiltonian of Eq. (1): the extrinsic RSOC and an EMF. The extrinsic RSOC lifts the corresponding bands' spin degeneracy, unless at $\mathbf{k} = 0$. Additionally, the EMF applied perpendicularly to the ribbon plane drives the system through TPTs exhibiting spin-polarized MZMs. In this situation, spin-discriminated MZMs emerge at the ends of the double-spin KzHNR structure. The corresponding generalized Hamiltonian is given by

$$H = H_t + H_\Delta + H_R + H_z, \quad (4)$$

which can be written in a new basis of four distinct atoms as indicated in Fig. 3.

On this basis, the Hamiltonian describing the NN hopping and the p -wave superconducting pairing reads

$$H_t = -\frac{\mu}{2} \sum_{i,\sigma} (a_{i\sigma}^\dagger a_{i\sigma} - a_{i\sigma} a_{i\sigma}^\dagger + b_{i\sigma}^\dagger b_{i\sigma} - b_{i\sigma} b_{i\sigma}^\dagger) + c_{i\sigma}^\dagger c_{i\sigma} - c_{i\sigma} c_{i\sigma}^\dagger + d_{i\sigma}^\dagger d_{i\sigma} - d_{i\sigma} d_{i\sigma}^\dagger)$$

$$\begin{aligned}
& - \frac{t}{4} \sum_i^M (a_{i\sigma}^\dagger b_{i\sigma} - b_{i\sigma} a_{i\sigma}^\dagger + b_{i\sigma}^\dagger c_{i\sigma} \\
& - c_{i\sigma} b_{i\sigma}^\dagger + d_{i\sigma}^\dagger c_{i\sigma} - c_{i\sigma} d_{i\sigma}^\dagger) \\
& - \sum_i^{M-1} \frac{t}{4} (a_{i\sigma}^\dagger b_{i+1\sigma} - b_{i+1\sigma} a_{i\sigma}^\dagger \\
& + d_{i\sigma}^\dagger c_{i+1\sigma} - c_{i+1\sigma} d_{i\sigma}^\dagger) + \text{H.c.} \quad (5)
\end{aligned}$$

and

$$\begin{aligned}
H_\Delta = \sum_i^{M-1} [\Delta (a_{i\sigma} a_{i+1\sigma} - a_{i+1\sigma} a_{i\sigma} \\
+ d_{i\sigma} d_{i+1\sigma} - d_{i+1\sigma} d_{i\sigma}) + \text{H.c.}], \quad (6)
\end{aligned}$$

respectively.

The extrinsic RSOC induced in the KzHNR can be generated by breaking the inversion symmetry due to either a substrate with strong spin-orbit interaction [15] or modulated by the action of an external electric field \vec{E} applied perpendicularly to the nanoribbon plane [38–40,42,61,62]. Its corresponding general Hamiltonian reads

$$H_R = \sum_{i,j,\sigma} [i a_{i,\sigma}^\dagger (\vec{u}_{ij} \cdot \vec{\sigma}) a_{j,\sigma} + \text{H.c.}], \quad (7)$$

where $\vec{u}_{ij} = (\frac{e}{2m^2 a v_f}) \vec{E} \times \vec{\delta}_{ij} = -\frac{\lambda_R}{a} \hat{k} \times \vec{\delta}_{ij}$, with e and m being the charge and mass of the electron, respectively. Moreover, v_f is the Fermi velocity, the lattice constant is given by a , and the vector-position $\vec{\delta}_{ij}$ corresponds to the three nearest neighbors, as represented in Fig. 1(b). Writing Eq. (7) in the basis defined in Fig. 3, we can write the Rashba Hamiltonian as

$$\begin{aligned}
H_R = \sum_{i,\sigma}^M i \lambda_R \text{sign}(\sigma) [\gamma_1 (a_{i\sigma}^\dagger b_{i\bar{\sigma}} - b_{i\sigma} a_{i\bar{\sigma}}^\dagger) \\
+ \left(-\frac{1}{2}\right) (b_{i\sigma}^\dagger c_{i\bar{\sigma}} - c_{i\sigma} b_{i\bar{\sigma}}^\dagger) + \gamma_2 (c_{i\sigma}^\dagger d_{i\bar{\sigma}} - d_{i\sigma} c_{i\bar{\sigma}}^\dagger)] \\
+ \sum_{i,\sigma}^{M-1} i \lambda_R \text{sign}(\sigma) [\gamma_2 (b_{i\sigma}^\dagger a_{i+1\bar{\sigma}} - a_{i+1\sigma} b_{i\bar{\sigma}}^\dagger) \\
+ \gamma_1 (d_{i\sigma}^\dagger c_{i+1\bar{\sigma}} - c_{i+1\sigma} d_{i\bar{\sigma}}^\dagger)] + \text{H.c.}, \quad (8)
\end{aligned}$$

where $\gamma_1 = (\frac{1}{2} + i\frac{\sqrt{3}}{2})$, $\gamma_2 = (\frac{1}{2} - i\frac{\sqrt{3}}{2})$, λ_R is the extrinsic RSOC parameter and $\sigma = \uparrow, \downarrow$ is the spin index for each operator. The last term of Eq. (4)

$$\begin{aligned}
H_z = \frac{1}{2} \sum_{i,\sigma}^M \lambda_Z \text{sign}(\sigma) [(a_{i,\sigma}^\dagger a_{i,\sigma} - a_{i,\sigma} a_{i,\sigma}^\dagger) \\
+ (b_{i,\sigma}^\dagger b_{i,\sigma} - b_{i,\sigma} b_{i,\sigma}^\dagger) + (c_{i,\sigma}^\dagger c_{i,\sigma} - c_{i,\sigma} c_{i,\sigma}^\dagger) \\
+ (d_{i,\sigma}^\dagger d_{i,\sigma} - d_{i,\sigma} d_{i,\sigma}^\dagger)] + \text{H.c.}, \quad (9)
\end{aligned}$$

represents an EMF with the magnetization vector pointing to the azimuthal direction [63,64], where λ_Z is the EMF strength.

Now, we perform a detailed analysis of how the KzHNR length M , the extrinsic RSOC λ_R , the superconducting pairing

Δ , and the EMF λ_Z affect the emergence of MZMs on the real axis. The Hamiltonian given by Eqs. (4)–(8) is solved numerically using the basis represented in Fig. 3. The calculation becomes more time-consuming as the Hamiltonian matrix dimension grows with the value of M .

In Figs. 4(I)–4(IV), we plot the energy spectra as a function of μ of a double-spin KzHNR with width $N = 2$ and length $M = 100$, for distinct parameters of the Hamiltonian: $\Delta = 0.5t$, $\lambda_R = 0.05t$, and $\lambda_Z = 0.1t$ except the corresponding varied parameter. We explicitly indicate it in the panels.

The emergence of polarized MZMs at the edges of the double-spin KzHNR is calculated by computing the mean value of $\langle S_z \rangle = \langle \psi | \hat{S}_z | \psi \rangle$ of MZMs solutions. The label ψ represents eigenvectors of the total Hamiltonian given by Eq. (4) and \hat{S}_z is the Pauli matrix in the \hat{z} direction.

Figure 4(I) shows the dependence of the energy spectra as a function of μ/t for lengths $M = 10$ (a), 50 (b), and 100 (c) of the double-spin KzHNR, respectively. In Fig. 4(a), we can verify oscillatory patterns for the smallest double-spin KzHNR structure. The oscillating behavior is expected to appear for short Majorana nanowires due to overlapping MZMs of opposite edges. For $M = 50$ [Fig. 4(b)], we observe the appearance of MZMs at the real axis around $\mu = 0$ and in the inferior band region in the range $\mu = [-1.2, -1.3]$. Figure 4(c) depicts the case of $M = 100$, showing the MZMs on the real axis in all the available topological regions.

Figure 4(II) shows the dependence of the energy spectra as a function of μ/t with the extrinsic RSOC parameters $\lambda_R = 0.01t, 0.03t$, and $0.05t$. The result shows that a low value of λ_R is sufficient to generate well-defined MZMs on the real axis in all the topological regions.

In Fig. 4(III), we observe the dependence of the energy spectra as a function of μ/t for $\Delta = 0.1t, 0.3t$, and $0.5t$, in Figs. 4(a)–4(c), respectively. These profiles indicate that the p -wave pairing Δ strongly affects the MZMs formation on the real axis. The MZMs are formed first for $\Delta = 0.1t$ [Fig. 4(a)] in the range $\mu = [-1.2, -1.3]$. Only when $\Delta = 0.5t$ [Fig. 4(b)] does the MZMs emerge around $\mu = 0$. Well-defined MZMs arises in the region of $\mu \simeq 0$ only for higher values of Δ .

Figure 4(IV) shows the dependence of the energy spectra with the EMF for $\lambda_Z = 0005t$ (a), $003t$ (b), and $008t$ (c) as a function of μ/t . The EMF acts uniformly over the MZMs formation for all μ values. The enhancement of λ_Z also increases the number of MZMs over the real axis.

The parameter analysis presented in Fig. 4 helps us to chose the parameters used in Fig. 5, which shows the high-resolution energy spectrum E/t of a finite double-spin KzHNR with $N = 2$, $M = 200$, $\Delta = 0.5t$, $\lambda_R = 0.05t$, and $\lambda_Z = 0.1t$ as a function of μ/t . Figure 5(a) has the same shape of the double-spinless case [Fig. 2(a)], but with spin-polarized energies resolved into spin-up (blue color) and spin-down (red color) regions at the real axis. A mirror spin-symmetry concerning $\mu = 0$ is observed in the plot: a spin-up MZMs for $\mu < 0$ changes to spin-down for $\mu > 0$. Moreover, spin-polarized MZMs can be accessed by tuning μ slightly below or above $\mu = 0$.

Figure 5(b) shows the enlarged region of Fig. 5(a) around $E = 0$ for $\mu < 0$, where it is possible to see in detail the emergence of spin-polarized MZMs as μ changes. We can

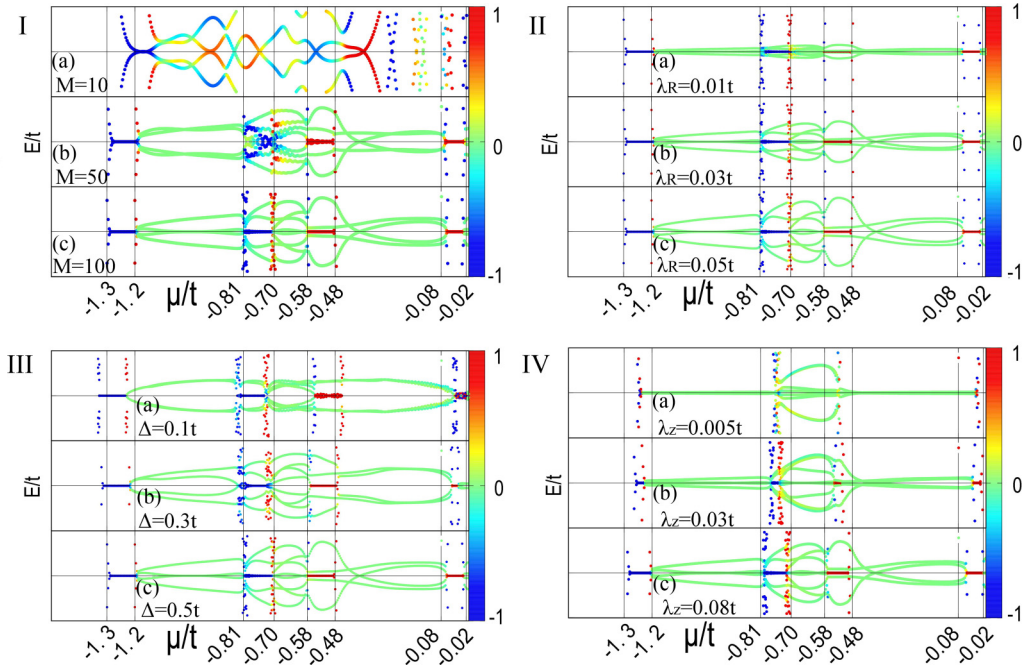


FIG. 4. Formation of MZMs parameter study: Energy spectra for a $N = 2$ finite double-spin KzHNR as a function of μ . We employed the same parameters set used in all the simulations of the paper: $\Delta = 0.5t$, $\lambda_R = 0.05t$, and $\lambda_Z = 0.1t$, but only changing the particular parameter indicated in the figure: (I) Length: $M = 10, 50, 100$. (II) Extrinsic Rashba spin-orbit coupling $\lambda_R = 0.01t, 0.03t, 0.05t$. (III) Superconductor pairing $\Delta = 0.1t, 0.3t, 0.5t$. (IV) EMF $\lambda_Z = 0.005t, 0.03, 0.08t$.

detect these MZMs with well-defined spin orientation via spin-polarized STM measurements [16]. The green lines depicted in both panels of Fig. 5 do not represent MZMs, but ordinary fermions, resulting from the combination of MZMs localized at the ends of opposite KzHNRs. This effect tends

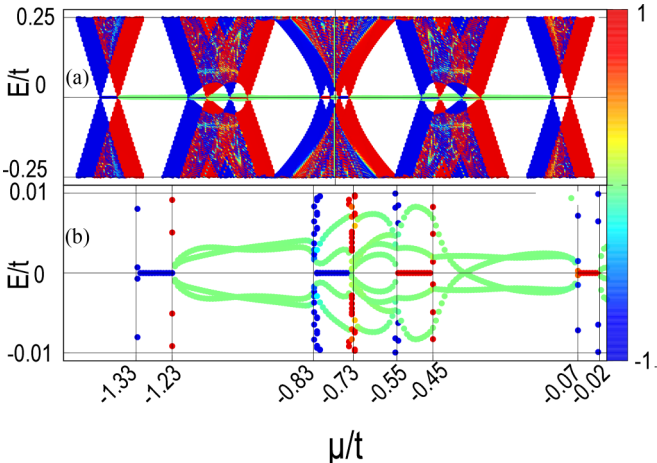


FIG. 5. (a) Energy spectra of a finite double-spin KzHNR [Eq. (4)] as a function of μ , $N = 2$, and $M = 200$. The model parameters are $\Delta = 0.5t$, $\lambda_R = 0.05t$, and $\lambda_Z = 0.1t$. The blue and red colors correspond to spin up and down regions at the real axis, respectively. The green lines describe the formation of a regular fermion coming from the combination of Majorana excitations belonging to opposite KzHNRs. (b) Enlarged region of (a) around $E = 0$ for $\mu < 0$, showing in detail the formation of spin-polarized MZMs.

to disappear as the width N of the double-spin KzHNR increases.

As discussed in the spinless case of Fig. 2, the emergence of spin-polarized MZMs on the real axis depicted in Fig. 5 is also related to TPTs in the bulk gap. However, each value of μ related to a TPT in the spinless scenario splits into two values of μ , describing TPTs for both spin-up and spin-down components. The strength of this splitting is given by the RSOC parameter λ_R . For details, see Fig. 6 and related discussion in Appendix A.

IV. EXPERIMENTAL PERSPECTIVES

Among available experimental results for realizing a double-spin KzHNR structure, we suggest the silicene deposited on a Pb superconducting substrate as a possible candidate. In the superconducting phase, under the presence of a strong RSOC coming from the Pb and an applied EMF, the Cooper pairs of the Pb substrate can enter into the silicene region via proximity effect, giving rise to a p -wave-induced pairing in the double KzHNR structure.

The growth of silicene under Pb substrates was experimentally investigated using guidelines of DFT simulations results [65–68]. However, the production of silicene nanoribbons inducing Pb reconstructions on Si(111) surface [69] was not successful. It was obtained short silicene-like nanoribbons directly bonded to the Si(111) layers, and Pb only acted as a surfactant.

A possible route to produce silicene nanoribbons [70] is to use Pb layers on vicinal Si surfaces [32–34], like Si(553) or Si(557). In the case of Pb/Si(553), Pb forms a dense layer. The Pb layer is electronically decoupled from the substrate to

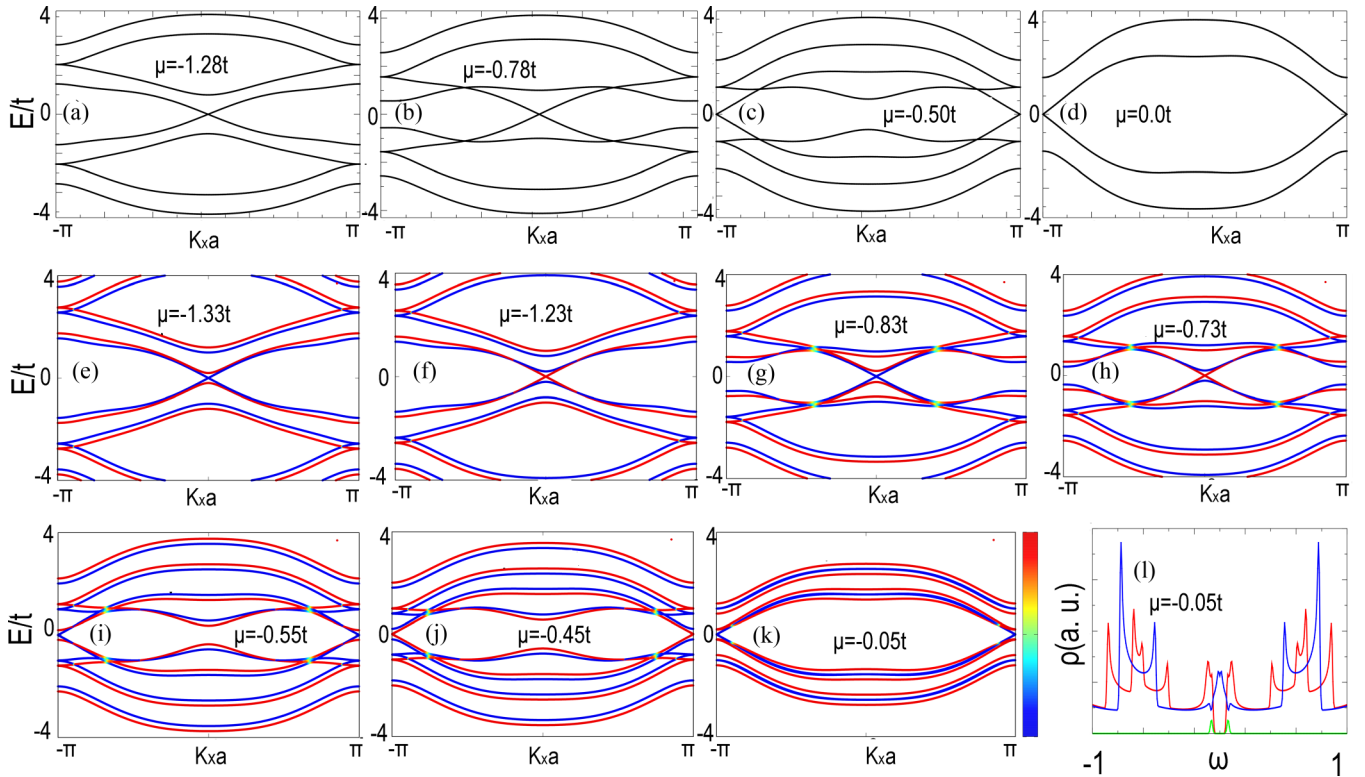


FIG. 6. Panels (a)–(d): band structure for a $N = 2$ infinity double-spinless KzHNR, considering μ values where the TPTs occur. Panels (e)–(k): the same as top panels, but considering both spin components (infinite double-spin KzHNR). The energies are measured in units of t as described in the main text, and we fix the p -wave superconducting pairing parameter $\Delta = 0.5t$. Additionally, the parameters of the double-spin case (middle and bottom panels) are $\lambda_R = 0.05t$ and $\lambda_Z = 0.1t$. In the double-spinless case, we have four TPTs occurring at (a) $\mu = -1.28t$, (b) $\mu = -0.78t$, (c) $\mu = -0.50t$, (d) $\mu = 0$. For the double-spin case, the TPTs occur at (e) $\mu = -1.33t$ with spin down, (f) $\mu = -1.23t$ with spin up, (g) $\mu = -0.84t$ with spin down, (h) $\mu = -0.73t$ with spin up, (i) $\mu = -0.55t$ with spin down, (j) $\mu = -0.45t$ with spin up, and (k) $\mu = -0.05t$ with spin down. The density of states, corresponding to the band structure depicted in panel (k), is plotted in panel (l), where we can observe the half-metallicity characteristic of those TPTs.

a large extent. This is entirely different from the case of Pb-induced Si(111) reconstruction. Strong Pb-Pb bonding within the layer should favor the growth of Si on it without migration of Pb atoms on top of silicene.

Moreover, several previous theoretical works have shown that the zHNRs accumulate electrons to form localized magnetic moments [71] at its edges. The coupling of atoms belonging to the same edge is ferromagnetic and between atoms from different edges is antiferromagnetic [72–75]. This situation is depicted in Fig. 1(c). In particular, narrow-width silicene nanoribbons are predicted to have an antiferromagnetic ground state [76,77]. Another possibility to experimentally realize a double-spin-polarized KzHNR is following the recipe of Ref. [15]: growing an antiferromagnetic nanoribbon or some artificial antiferromagnetic ladder over a strong spin-orbit conventional s -wave superconductor. In Appendix B, we present an estimative about the possibilities to experimentally realize a double-spin KzHNR based on silicene layers deposited on top of a Pb superconducting substrate.

V. CONCLUSIONS

This work reports the possibility of obtaining spin-polarized MZMs at opposite edges of a double-spin KzHNR

structure. The regions of energy spectrum E/t with MZMs having well-defined either spin-up or spin-down orientations can be accessed by tuning the μ/t of the KzHNRs. Moreover, these spin-polarized intervals in the $E/t \times \mu/t$ profile are associated with distinct topological phases, characterized by the topological invariant winding number $W = 1$ or $W = 2$. Interestingly enough, for the situation wherein $W = 2$ four MZMs emerge in the double KzHNR geometry: two at the opposite ends of the top zHNR and two at the opposite ends of the bottom one. In this scenario, it should be emphasized that at least four MZMs are required for defining a qubit [78–81]. Thus, the proposal is a natural candidate for realizing hybrid quantum computing operations [52,53] between conventional spin qubits and topological qubits based on MZMs with well-defined spin orientation, suggesting a possible route for performing Majorana spintronics.

ACKNOWLEDGMENTS

We acknowledge the support from Brazilian National Council for Scientific and Technological Development (CNPq) and Coordenação de Aperfeiçoamento de Pessoal de Nível Superior–Brasil (CAPES). M.S.F. Acknowledges financial support from the Brazilian agencies FAPERJ Process

No. 210 355/2018 and CNPq Grant No. 311980/2021-0. L.S.R. acknowledges the Icelandic Research Fund (Project ‘‘Hybrid Polaritonics’’). A.C.S. acknowledges CNPq Grant No. 305668/2018-8.

APPENDIX A: INFINITE DOUBLE KZHNR

1. Spinless case

In this Appendix, we will consider the infinite double KzHNR case. We are interested in calculating the winding numbers, the band structure, and the topological phase transitions exhibited by the system. In the main text of the work, we use this information as guidelines to interpret the emergence of MZMs in the finite case. By considering the Fourier transform of Eqs. (2) and (3), the total Hamiltonian can be written as

$$H = H_t + H_\Delta, \quad (\text{A1})$$

with the first nearest neighbor hopping and the superconductor pairing term. In the momentum representation, the Hamiltonian can be written as

$$H_t = - \sum_{k,n} [\mu(a_{k,n}^\dagger a_{k,n} + b_{k,n}^\dagger b_{k,n}) + t(a_{k,n}^\dagger b_{k,n-1} - 2a_{k,n}^\dagger b_{k,n} \cos(ka/2)) + \text{H.c.}],$$

$$H_\Delta = \sum_{k,n} [2i\Delta \sin(k)(a_{k,n}^\dagger a_{-k,n}^\dagger + b_{k,n+1}^\dagger b_{-k,n+1}^\dagger) + \text{H.c.}], \quad (\text{A2})$$

where $n = 1, 2$, corresponding to the top and bottom chain index. In the Bogoliubov–de Gennes (BdG) form, we can express the Hamiltonian as $\frac{1}{2} \sum_k \Psi^\dagger h(k) \Psi$, with $\Psi \equiv (a_{k,1}, a_{-k,1}^\dagger, b_{k,1}, b_{-k,1}^\dagger, a_{k,2}, a_{-k,2}^\dagger, b_{k,2}, b_{-k,2}^\dagger)$. We obtain the

$$A(k) = \begin{bmatrix} -4i\Delta \sin(k) + 4\mu & -4t \cos(\frac{k}{2}) & 0 & 0 \\ -4t \cos(\frac{k}{2}) & -4i\Delta \sin(k) + 4\mu & 2t & 0 \\ 0 & 2t & -4i\Delta \sin(k) + 4\mu & -4t \cos(\frac{k}{2}) \\ 0 & 0 & -4t \cos(\frac{k}{2}) & -4i\Delta \sin(k) + 4\mu \end{bmatrix}. \quad (\text{A9})$$

Once particle-hole, time-reversal, and chiral symmetries are preserved by $h(k)$, the corresponding system belongs to the BDI symmetry group class with \mathbb{Z} index [57,58], with its topology being characterized by the associated Chern number invariant [82], i.e., the winding number [55,56]

$$W = \text{Tr} \int_{-\pi}^{\pi} \frac{dk}{2\pi i} A_k^{-1} \partial_k A_k = - \int_{-\pi}^{\pi} \frac{dk}{2\pi i} \partial_k \ln[\text{Det}(A_k)], \quad (\text{A10})$$

total Hamiltonian in the following matrix form,

$$h(k) = \begin{pmatrix} -2\mu & \Delta_k & -\epsilon & 0 & 0 & 0 & 0 & 0 \\ \Delta_k^* & +2\mu & 0 & \epsilon & 0 & 0 & 0 & 0 \\ -\epsilon & 0 & -2\mu & \Delta_k & -t & 0 & 0 & 0 \\ 0 & \epsilon & \Delta_k^* & +2\mu & 0 & t & 0 & 0 \\ 0 & 0 & -t & 0 & -2\mu & \Delta_k & -\epsilon & 0 \\ 0 & 0 & 0 & t & \Delta_k^* & +2\mu & 0 & \epsilon \\ 0 & 0 & 0 & 0 & -\epsilon & 0 & -2\mu & \Delta_k \\ 0 & 0 & 0 & 0 & 0 & \epsilon & \Delta_k^* & +2\mu \end{pmatrix}, \quad (\text{A3})$$

where $\Delta_k = 2i\Delta \sin(k)$ and $\epsilon = -2t \cos(k/2)$. This Hamiltonian has the dispersion relations given by

$$E_{1,2,3,4} = \pm \sqrt{\frac{-2\Delta^2 + 2\zeta_1 + t^2 \pm \tilde{\epsilon}(4\mu + t)}{2}},$$

$$E_{5,6} = \pm \sqrt{\frac{-2\Delta^2 + 2\zeta_2 + t^2 - \tilde{\epsilon}(4\mu - t)}{2}}, \quad (\text{A4})$$

$$\text{and } E_{7,8} = \pm \sqrt{-\Delta^2 + \epsilon^2 + 2\zeta_3 + \tilde{\epsilon}(2\mu - t/2)},$$

with $\zeta_1 = \epsilon^2 + 2\mu^2 + 2\mu t$, $\zeta_2 = \epsilon^2 + 4\mu^2 - 2\mu t$, $\zeta_3 = 2\mu^2 - \mu t + t^2$, and $\tilde{\epsilon} = \sqrt{4\epsilon^2 + t^2}$. It is worth noting that Eq. (A3) satisfies both the particle-hole and time-reversal symmetries, since

$$\mathcal{C}h(k)\mathcal{C}^{-1} = -h(-k) \quad (\text{A5})$$

and

$$\mathcal{T}h(k)\mathcal{T}^{-1} = h(-k), \quad (\text{A6})$$

where \mathcal{C} and \mathcal{T} are charge conjugation and time-reversal operators [57,58], respectively. Equation (A3) also satisfies the chiral symmetry

$$\mathcal{K}h(k)\mathcal{K}^{-1} = -h(k), \quad (\text{A7})$$

in which the chiral operator is defined by the anticommutation relation $[\mathcal{K}, h(k)]_+ = 0$. Thus, one can write $h(k)$ in its corresponding chiral form by performing the following unitary transformation:

$$\tilde{h}(k) = \mathcal{U}^\dagger h(k) \mathcal{U} = \begin{bmatrix} 0 & A(k) \\ A^*(k) & 0 \end{bmatrix}, \quad (\text{A8})$$

where $A(k)$ is a 4×4 chiral matrix given by

which gives the number of MZMs at the edges of the spinless KzHNR, as discussed in Fig. 2.

In Figs. 6(a)–6(d), we plot the band relation dispersion [Eq. (A4)] for a $N = 2$ infinity double-spinless KzHNR, considering μ/t values where the TPTs occur. For [Fig. 6(a)] $\mu = -1.28t$ and for [Fig. 6(b)] $\mu = -0.78t$, the gap closes at $k = 0$, defining two TPTs and forming a topological phase in this interval with winding number equal to $W = 1$. A new TPT occurs at [Fig. 6(c)] $\mu = -0.50t$, with the gap closing

at $\vec{k} = \pi$, and defining a new topological region with winding number equal to $W = 2$ between $\mu = -0.78t$ and $\mu = -0.50t$. Finally, at [Fig. 6(d)] $\mu = 0$ the gap closes again at $\vec{k} = \pi$, defining another TPT, and forming a topological phase with winding number equal to $W = 1$ between $\mu = -0.50t$ and $\mu = 0$. The same transitions appear at the same values for positive chemical potentials, once the system described by Eq. (A3) exhibits a particle-hole symmetry.

2. Spinfull case

Considering the Fourier transform of the total Hamiltonian given by Eq. 4, we calculate the topological phase transitions for the infinite spinfull case as a function of the chemical potential. By considering again $n = 1, 2$, as the top and bottom chain indexes,

$$H_t = - \sum_{k,n,\sigma}^N \mu (a_{k,n,\sigma}^\dagger a_{k,n,\sigma} + b_{k,n,\sigma}^\dagger b_{k,n,\sigma}) + t (a_{k,n,\sigma}^\dagger b_{k,n-1,\sigma} - 2a_{k,n,\sigma}^\dagger b_{k,n,\sigma} \cos(ka/2)) + \text{H.c.}, \quad (\text{A11})$$

$$H_\Delta = \sum_{k,n,\sigma}^N \Delta_k (a_{k,n,\sigma}^\dagger a_{-k,n,\sigma}^\dagger + b_{k,n+1,\sigma}^\dagger b_{-k,n+1,\sigma}^\dagger) + \text{H.c.}, \quad (\text{A12})$$

$$\Delta_k = 2i\Delta \sin(k),$$

$$H_R = \sum_{k,n,\sigma}^N \Lambda_{R\sigma} \left[-a_{k,n,\sigma}^\dagger b_{k,n-1,\bar{\sigma}} - 2 \cos\left(k/2 - \frac{2\pi}{3}\right) a_{k,n,\sigma}^\dagger b_{k,n,\bar{\sigma}} + b_{k,n,\sigma}^\dagger a_{k,n+1,\bar{\sigma}} + 2 \cos\left(k/2 + \frac{2\pi}{3}\right) b_{k,n,\sigma}^\dagger a_{k,n,\bar{\sigma}} \right] + \text{H.c.}, \quad (\text{A13})$$

$$\Lambda_{R\sigma} = i\lambda_R \text{sign}(\sigma),$$

and

$$H_z = \sum_{k,n,\sigma}^N \text{sign}(\sigma) \lambda_Z (a_{k,n,\sigma}^\dagger a_{k,n,\sigma} + b_{k,n,\sigma}^\dagger b_{k,n,\sigma}) + \text{H.c.} \quad (\text{A14})$$

In Figs. 6(e)–6(k), we plot the band structure [Eqs. (A11)–(A14)] for a $N = 2$ infinity double-spin KzHNR, considering μ values where the TPTs occur. To discriminate the two possible spin orientations in the edges of the KzHNR, we introduce two new physical effects: the extrinsic RSOC and the EMF given by Eqs. (A13) and (A14). When compared to the previous case, each transition splits into two, one with spin up and the other with spin down, where the split is tuned

by the $\lambda_R = \pm 0.05t$ parameter. For example, the TPT that occurs at Fig. 6(a) $\mu = -1.28t$, for the spinless case splits into $\mu \rightarrow \mu \pm \lambda_R = -1.33t; -1.23t$ in Figs. 6(e) and 6(f), respectively. However, in the double-spin case, we did not obtain the winding numbers due to the involved complexity of the calculations.

In Fig. 6(l), we plot a typical density of states for $\mu = -0.05t$ in a point where a TPT occurs and that exhibits half-metallicity, which is another striking characteristic that occurs in all the other Majorana TPTs of the system. This effect leads the double-spin KzHNR into a half-metallic state as indicated in Fig. 6(l), resulting in insulating behavior for one spin component and metallic behavior for the other component [83,84].

APPENDIX B: EXPERIMENTAL PROSPECTS ABOUT A DOUBLE-SPIN KZHNR BASED ON SILICENE LAYERS DEPOSITED ON TOP OF A PB SUPERCONDUCTING SUBSTRATE

Silicene layers were grown on Ag, Ir, Ca, and Pb, among other metallic substrates [85]. However, due to the considerable band hybridization between silicene and the substrate, the absence of Dirac cones is a characteristic feature, except for Ca and Pb, which preserves the Dirac cone below the Fermi surface [65]. Interesting enough, Pb is a conventional Bardeen-Cooper-Schrieffer (BCS) superconductor, with a relatively high critical temperature of $T_C = 7.2$ K and a strong intrinsic RSOC around 1 meV [37].

Due to its buckled structure and large silicon ionic radius, silicene has a relatively large effective intrinsic spin-orbit coupling of 1.55 meV, and an intrinsic RSOC of 0.7 meV [37]. However, this intrinsic RSOC is not enough to break the spin degeneracy of the energy spectra. Based on Ref. [17], we estimate the corresponding parameters for a silicene double-spin KzHNR structure on top of a Pb superconducting substrate.

To develop a topological phase in the silicene-Pb superconducting hybrid structure, the Zeeman energy λ_Z should satisfy the relation $\lambda_Z > \sqrt{\Delta_{\text{ind}}^2 + \mu^2}$, where Δ_{ind}^2 is the induced superconducting gap in the silicene layers due to proximity effect and $\lambda_Z = \frac{1}{2} g_{\text{Si}} \mu_B B$, with the silicene g factor g_{Si} and the Bohr magneton μ_B . On the other hand, the Pb superconducting quasiparticle excitation spectrum exhibits a gap of width $E_g = 2\Delta_S \simeq 2.73$ meV around the Fermi level [86], with Δ_S being the binding energy of the Cooper pairs. Thus, λ_Z should not assume values bigger than Pb superconducting energy gap, i.e., $\frac{1}{2} g_{\text{Pb}} \mu_B B < E_g$. Considering $g_{\text{Si}} \simeq 2.0$ associated to the free-electron silicene conduction band and $g_{\text{Pb}} = 1.5$, associated to the 3P_1 configuration of Pb [87], we estimate that $3.64 \text{ meV} > \sqrt{\Delta_{\text{ind}}^2 + \mu^2}$, which turns our proposal feasible from the experimental point of view.

[1] N. Read and D. Green, Paired states of fermions in two dimensions with breaking of parity and time-reversal symmetries

and the fractional quantum Hall effect, *Phys. Rev. B* **61**, 10267 (2000).

- [2] A. Y. Kitaev, Unpaired Majorana fermions in quantum wires, *Phys. Usp.* **44**, 131 (2001).
- [3] Y. Oreg, G. Refael, and F. von Oppen, Helical Liquids and Majorana Bound States in Quantum Wires, *Phys. Rev. Lett.* **105**, 177002 (2010).
- [4] R. M. Lutchyn, J. D. Sau, and S. Das Sarma, Majorana Fermions and a Topological Phase Transition in Semiconductor-Superconductor Heterostructures, *Phys. Rev. Lett.* **105**, 077001 (2010).
- [5] V. Mourik, K. Zuo, S. M. Frolov, S. R. Plissard, E. P. A. M. Bakkers, and L. P. Kouwenhoven, Signatures of Majorana fermions in hybrid superconductor-semiconductor nanowire devices, *Science* **336**, 1003 (2012).
- [6] Ö. Gül, H. Zhang, J. D. S. Bommer, M. W. A. de Moor, D. Car, S. R. Plissard, E. P. A. M. Bakkers, A. Geresdi, K. Watanabe, T. Taniguchi, and L. P. Kouwenhoven, Ballistic Majorana nanowire devices, *Nat. Nanotechnol.* **13**, 192 (2018).
- [7] R. Aguado, Majorana quasiparticles in condensed matter, *Riv Nuovo Cimento* **40**, 523 (2017).
- [8] P. Krogstrup, N. L. B. Ziino, W. Chang, S. M. Albrecht, M. H. Madsen, E. Johnson, J. Nygård, C. M. Marcus, and T. S. Jespersen, Epitaxy of semiconductor–superconductor nanowires, *Nat. Mater.* **14**, 400 (2015).
- [9] D. J. Clarke, Experimentally accessible topological quality factor for wires with zero energy modes, *Phys. Rev. B* **96**, 201109(R) (2017).
- [10] A. Schuray, L. Weithofer, and P. Recher, Fano resonances in Majorana bound states–quantum dot hybrid systems, *Phys. Rev. B* **96**, 085417 (2017).
- [11] E. Prada, R. Aguado, and P. San-Jose, Measuring Majorana nonlocality and spin structure with a quantum dot, *Phys. Rev. B* **96**, 085418 (2017).
- [12] L. S. Ricco, M. de Souza, M. S. Figueira, I. A. Shelykh, and A. C. Seridonio, Spin-dependent zero-bias peak in a hybrid nanowire-quantum dot system: Distinguishing isolated Majorana fermions from Andreev bound states, *Phys. Rev. B* **99**, 155159 (2019).
- [13] M. T. Deng, S. Vaitiekėnas, E. B. Hansen, J. Danon, M. Leijnse, K. Flensberg, J. Nygård, P. Krogstrup, and C. M. Marcus, Majorana bound state in a coupled quantum-dot hybrid-nanowire system, *Science* **354**, 1557 (2016).
- [14] M.-T. Deng, S. Vaitiekėnas, E. Prada, P. San-Jose, J. Nygård, P. Krogstrup, R. Aguado, and C. M. Marcus, Nonlocality of Majorana modes in hybrid nanowires, *Phys. Rev. B* **98**, 085125 (2018).
- [15] S. Nadj-Perge, I. K. Drozdov, J. Li, H. Chen, S. Jeon, J. Seo, A. H. MacDonald, B. A. Bernevig, and A. Yazdani, Observation of Majorana fermions in ferromagnetic atomic chains on a superconductor, *Science* **346**, 602 (2014).
- [16] S. Jeon, Y. Xie, J. Li, Z. Wang, B. A. Bernevig, and A. Yazdani, Distinguishing a Majorana zero mode using spin-resolved measurements, *Science* **358**, 772 (2017).
- [17] K. Flensberg, F. von Oppen, and A. Stern, Engineered platforms for topological superconductivity and Majorana zero modes, *Nat. Rev. Mater.* **6**, 944 (2021).
- [18] J. Berthold, X. Yonglong, and A. Yazdani, Detecting and distinguishing majorana zero modes with the scanning tunnelling microscope, *Nat. Rev. Phys.* **3**, 541 (2021).
- [19] H. Zhang, D. E. Liu, M. Wimmer, and L. P. Kouwenhoven, Next steps of quantum transport in Majorana nanowire devices, *Nat. Commun.* **10**, 5128 (2019).
- [20] E. Prada, P. San-Jose, M. W. A. de Moor, A. Geresdi, E. J. H. Lee, J. Klinovaja, D. Loss, J. Nygård, R. Aguado, and L. P. Kouwenhoven, From Andreev to Majorana bound states in hybrid superconductor-semiconductor nanowires, *Nat. Rev. Phys.* **2**, 575 (2020).
- [21] P. Yu, J. Chen, M. Gomanko, G. Badawy, E. P. A. M. Bakkers, K. Zuo, V. Mourik, and S. M. Frolov, Non-Majorana states yield nearly quantized conductance in superconductor-semiconductor nanowire devices, *Nat. Phys.* **17**, 482 (2021).
- [22] P. Yu, B. D. Woods, J. Chen, G. Badawy, E. P. A. M. Bakkers, T. D. Stanescu, and S. M. Frolov, Delocalized states in three-terminal superconductor-semiconductor nanowire devices, [arXiv:2108.07327](https://arxiv.org/abs/2108.07327) [cond-mat.mes-hall].
- [23] M. Pendharkar, B. Zhang, H. Wu, A. Zarassi, P. Zhang, C. P. Dempsey, J. S. Lee, S. D. Harrington, G. Badawy, S. Gazibegovic, R. L. M. O. het Veld, M. Rossi, J. Jung, A.-H. Chen, M. A. Verheijen, M. Hocevar, E. P. A. M. Bakkers, C. J. Palmström, and S. M. Frolov, Parity-preserving and magnetic field-resilient superconductivity in InSb nanowires with Sn shells, *Science* **372**, 508 (2021).
- [24] H. Pan and S. Das Sarma, Physical mechanisms for zero-bias conductance peaks in Majorana nanowires, *Phys. Rev. Research* **2**, 013377 (2020).
- [25] H. Pan, W. S. Cole, J. D. Sau, and S. Das Sarma, Generic quantized zero-bias conductance peaks in superconductor-semiconductor hybrid structures, *Phys. Rev. B* **101**, 024506 (2020).
- [26] H. Pan, C.-X. Liu, M. Wimmer, and S. Das Sarma, Quantized and unquantized zero-bias tunneling conductance peaks in Majorana nanowires: Conductance below and above $2e^2/h$, *Phys. Rev. B* **103**, 214502 (2021).
- [27] J. Klinovaja, G. J. Ferreira, and D. Loss, Helical states in curved bilayer graphene, *Phys. Rev. B* **86**, 235416 (2012).
- [28] J. Klinovaja and D. Loss, Giant Spin-Orbit Interaction Due to Rotating Magnetic Fields in Graphene Nanoribbons, *Phys. Rev. X* **3**, 011008 (2013).
- [29] A. Zhaao and B. Wang, Two-dimensional graphene-like Xenes as potential topological materials, *APL Mater.* **8**, 030701 (2020).
- [30] C. Dutreix, M. Guigou, D. Chevallier, and C. Bena, Majorana fermions in honeycomb lattices, *Eur. Phys. J. B* **87**, 296 (2014).
- [31] T. Ma, F. Yang, Z. Huang, and H.-Q. Lin, Triplet p -wave pairing correlation in low-doped zigzag graphene nanoribbons, *Sci. Rep.* **7**, 42262 (2017).
- [32] M. Kopciuszynski, P. Dyniec, M. Krawiec, P. Łukasik, M. Jałochowski, and R. Zdyb, Pb nanoribbons on the Si(553) surface, *Phys. Rev. B* **88**, 155431 (2013).
- [33] M. Kopciuszynski, M. Krawiec, R. Zdyb, and M. Jałochowski, Purely one-dimensional bands with a giant spin-orbit splitting: Pb nanoribbons on Si(553) surface, *Sci. Rep.* **7**, 46215 (2017).
- [34] C. Brand, S. Muff, M. Fanciulli, H. Pfñür, M. C. Tringides, J. H. Dil, and C. Tegenkamp, Spin-resolved band structure of a densely packed Pb monolayer on Si(111), *Phys. Rev. B* **96**, 035432 (2017).
- [35] B. Lalmi, H. Oughaddou, H. Enriquez, A. Kara, S. Vizzini, B. Ealet, and B. Aufray, Epitaxial growth of a silicene sheet, *Appl. Phys. Lett.* **97**, 223109 (2010).

- [36] B. Aufray, A. Kara, S. Vizzini, H. Oughaddou, C. Léandri, B. Ealet, and G. Le Lay, Graphene-like silicon nanoribbons on Ag(110): A possible formation of silicene, *Appl. Phys. Lett.* **96**, 183102 (2010).
- [37] C.-C. Liu, H. Jiang, and Y. Yao, Low-energy effective Hamiltonian involving spin-orbit coupling in silicene and two-dimensional germanium and tin, *Phys. Rev. B* **84**, 195430 (2011).
- [38] M. Ezawa, Valley-Polarized Metals and Quantum Anomalous Hall Effect in Silicene, *Phys. Rev. Lett.* **109**, 055502 (2012).
- [39] N. D. Drummond, V. Zólyomi, and V. I. Fal'ko, Electrically tunable band gap in silicene, *Phys. Rev. B* **85**, 075423 (2012).
- [40] Z. Jiao, Q. Yao, and H. Zandvliet, Tailoring and probing the quantum states of matter of 2d Dirac materials with a buckled honeycomb structure, *Phys. E* **121**, 114113 (2020).
- [41] W.-F. Tsai, C.-Y. Huang, T.-R. Chang, H. Lin, H.-T. Jeng, and A. Bansil, Gated silicene as a tunable source of nearly 100% spin-polarized electrons, *Nat. Commun.* **4**, 1500 (2013).
- [42] L. Chico, A. Latgé, and L. Brey, Symmetries of quantum transport with Rashba spin orbit: Graphene spintronics, *Phys. Chem. Chem. Phys.* **17**, 16469 (2015).
- [43] P. Jiang, L. Kang, X. Tao, N. Cao, H. Hao, X. Zheng, L. Zhang, and Z. Zeng, Robust generation of half-metallic transport and pure spin current with photogalvanic effect in zigzag silicene nanoribbons, *J. Phys.: Condens. Matter* **31**, 495701 (2019).
- [44] T.-C. Wang, C.-H. Hsu, Z.-Q. Huang, F.-C. Chuang, W.-S. Su, and G.-Y. Guo, Tunable magnetic states on the zigzag edges of hydrogenated and halogenated group-IV nanoribbons, *Sci. Rep.* **6**, 39083 (2016).
- [45] J. F. Silva, L. G. V. Dias da Silva, and E. Vernek, Robustness of the Kondo effect in a quantum dot coupled to Majorana zero modes, *Phys. Rev. B* **101**, 075428 (2020).
- [46] A. Schuray, M. Rammler, and P. Recher, Signatures of the Majorana spin in electrical transport through a Majorana nanowire, *Phys. Rev. B* **102**, 045303 (2020).
- [47] L. Fu and C. L. Kane, Superconducting Proximity Effect and Majorana Fermions at the Surface of a Topological Insulator, *Phys. Rev. Lett.* **100**, 096407 (2008).
- [48] Y. Nagai, H. Nakamura, and M. Machida, Spin-polarized Majorana bound states inside a vortex core in topological superconductors, *J. Phys. Soc. Jpn.* **83**, 064703 (2014).
- [49] J.-P. Xu, M.-X. Wang, Z. L. Liu, J.-F. Ge, X. Yang, C. Liu, Z. A. Xu, D. Guan, C. L. Gao, D. Qian, Y. Liu, Q.-H. Wang, F.-C. Zhang, Q.-K. Xue, and J.-F. Jia, Experimental Detection of a Majorana Mode in the Core of a Magnetic Vortex Inside a Topological Insulator-Superconductor $\text{Bi}_2\text{Te}_3/\text{NbSe}_2$ Heterostructure, *Phys. Rev. Lett.* **114**, 017001 (2015).
- [50] E. D. B. Smith, K. Tanaka, and Y. Nagai, Manifestation of chirality in the vortex lattice in a two-dimensional topological superconductor, *Phys. Rev. B* **94**, 064515 (2016).
- [51] K. K. Tanaka, M. Ichioka, and S. Onari, Spin-polarized local density of states in the vortex state of helical p -wave superconductors, *Phys. Rev. B* **95**, 134502 (2017).
- [52] M. Leijnse and K. Flensberg, Quantum Information Transfer Between Topological and Spin Qubit Systems, *Phys. Rev. Lett.* **107**, 210502 (2011).
- [53] M. Leijnse and K. Flensberg, Hybrid topological-spin qubit systems for two-qubit-spin gates, *Phys. Rev. B* **86**, 104511 (2012).
- [54] S. Hoffman, C. Schrade, J. Klinovaja, and D. Loss, Universal quantum computation with hybrid spin-Majorana qubits, *Phys. Rev. B* **94**, 045316 (2016).
- [55] B.-Z. Zhou, D.-H. Xu, and B. Zhou, Majorana zero modes in a ladder of density-modulated Kitaev superconductor chains, *Phys. Lett. A* **381**, 2426 (2017).
- [56] A. Maiellaro, F. Romeo, and R. Citro, Topological phase diagram of a Kitaev ladder, *Eur. Phys. J.: Spec. Top.* **227**, 1397 (2018).
- [57] C.-K. Chiu, J. C. Y. Teo, A. P. Schnyder, and S. Ryu, Classification of topological quantum matter with symmetries, *Rev. Mod. Phys.* **88**, 035005 (2016).
- [58] R. Wakatsuki, M. Ezawa, and N. Nagaosa, Majorana fermions and multiple topological phase transition in Kitaev ladder topological superconductors, *Phys. Rev. B* **89**, 174514 (2014).
- [59] A. Alase, *Boundary Physics and Bulk-Boundary Correspondence in Topological Phases of Matter*, 1st ed., Springer Theses (Springer Nature Switzerland AG, 2019).
- [60] It also should be noticed in Fig. 2(a) that there is an uncharacterized small region in the interval $-0.02t < \mu < 0.02t$, which is an effect produced by the finite length of the KzHNR chain considered in the calculations ($M = 200$) and therefore tends to disappear for larger values of M , giving rise to a single TPT at $\mu = 0$.
- [61] H. Min, J. E. Hill, N. A. Sinitsyn, B. R. Sahu, L. Kleinman, and A. H. MacDonald, Intrinsic and Rashba spin-orbit interactions in graphene sheets, *Phys. Rev. B* **74**, 165310 (2006).
- [62] M. Zarea and N. Sandler, Rashba spin-orbit interaction in graphene and zigzag nanoribbons, *Phys. Rev. B* **79**, 165442 (2009).
- [63] G. S. Diniz, M. R. Guassi, and F. Qu, Controllable spin-charge transport in strained graphene nanoribbon devices, *J. Appl. Phys.* **116**, 113705 (2014).
- [64] W.-K. Tse, Z. Qiao, Y. Yao, A. H. MacDonald, and Q. Niu, Quantum anomalous Hall effect in single-layer and bilayer graphene, *Phys. Rev. B* **83**, 155447 (2011).
- [65] A. Podsiadly-Paszowska and M. Krawiec, Silicene on metallic quantum wells: An efficient way of tuning silicene-substrate interaction, *Phys. Rev. B* **92**, 165411 (2015).
- [66] M. Stepniak-Dybala, Jalochoowski and M. Krawiec, Silicene nanoribbons on Pb-reconstructed Si(111) surface, *Condens. Matter* **1**, 8 (2016).
- [67] A. Stepniak-Dybala and M. Krawiec, Formation of silicene on ultrathin Pb(111) films, *J. Phys. Chem. C* **123**, 17019 (2019).
- [68] S. Owczarek and L. Markowski, The role of surfactant in two-components structures formation on Si(111) surface, *Surf. Sci.* **693**, 121552 (2020).
- [69] M. Stepniak-Dybala, A. Krawiec, Structural model of silicene-like nanoribbons on a Pb-reconstructed Si(111) surface, *Beilstein J. Nanotechnol.* **8**, 1836 (2017).
- [70] M. Krawiec (private communication).
- [71] K. Nakada, M. Fujita, G. Dresselhaus, and M. S. Dresselhaus, Edge state in graphene ribbons: Nanometer size effect and edge shape dependence, *Phys. Rev. B* **54**, 17954 (1996).
- [72] K. Wakabayashi, K. Sasaki, T. Nakanishi, and T. Enoki, Electronic states of graphene nanoribbons and analytical solutions, *Sci. Technol. Adv. Mat.* **11**, 054504 (2010).

- [73] B. Fu, M. Abid, and C.-C. Liu, Systematic study on stanene bulk states and the edge states of its zigzag nanoribbon, *New J. Phys.* **19**, 103040 (2017).
- [74] J. H. Correa, A. Pezo, and M. S. Figueira, Braiding of edge states in narrow zigzag graphene nanoribbons: Effects of third-neighbor hopping on transport and magnetic properties, *Phys. Rev. B* **98**, 045419 (2018).
- [75] X. Zhu, H. Guo, and S. Feng, Quantum magnetism of topologically-designed graphene nanoribbons, *J. Phys.: Condens. Matter* **31**, 505601 (2019).
- [76] C. Xu, G. Luo, Q. Liu, J. Zheng, Z. Zhang, S. Nagase, Z. Gao, and J. Lu, Giant magnetoresistance in silicene nanoribbons, *Nanoscale* **4**, 3111 (2012).
- [77] X. L. Lu, Y. Xie, and H. Xie, Topological and magnetic phase transition in silicene-like zigzag nanoribbons, *New J. Phys.* **20**, 043054 (2018).
- [78] T. Karzig, C. Knapp, R. M. Lutchyn, P. Bonderson, M. B. Hastings, C. Nayak, J. Alicea, K. Flensberg, S. Plugge, Y. Oreg, C. M. Marcus, and M. H. Freedman, Scalable designs for quasiparticle-poisoning-protected topological quantum computation with majorana zero modes, *Phys. Rev. B* **95**, 235305 (2017).
- [79] C. Nayak, S. H. Simon, A. Stern, M. Freedman, and S. Das Sarma, Non-Abelian anyons and topological quantum computation, *Rev. Mod. Phys.* **80**, 1083 (2008).
- [80] J. F. Steiner and F. von Oppen, Readout of Majorana qubits, *Phys. Rev. Research* **2**, 033255 (2020).
- [81] D. Aasen, M. Hell, R. V. Mishmash, A. Higginbotham, J. Danon, M. Leijnse, T. S. Jespersen, J. A. Folk, C. M. Marcus, K. Flensberg, and J. Alicea, Milestones Toward Majorana-Based Quantum Computing, *Phys. Rev. X* **6**, 031016 (2016).
- [82] B. A. Bernevig and T. L. Hughes, *Topological Insulators and Topological Superconductors*, student (ed.) (Princeton University Press, Princeton, NJ, 2013).
- [83] F. Khoeini, K. Shakouri, and F. M. Peeters, Peculiar half-metallic state in zigzag nanoribbons of MoS₂: Spin filtering, *Phys. Rev. B* **94**, 125412 (2016).
- [84] R. Xu, B. Liu, X. Zou, and H.-M. Cheng, Half-metallicity in Co-doped WSe₂ nanoribbons, *ACS Appl. Mater. Interfaces* **9**, 38796 (2017).
- [85] H.-X. Zhong, R.-G. Quhe, Y.-Y. Wang, J.-J. Shi, and J. Lu, Silicene on substrates: A theoretical perspective, *Chin. Phys. B* **24**, 087308 (2015).
- [86] M. Ruby, B. W. Heinrich, J. I. Pascual, and K. J. Franke, Experimental Demonstration of a Two-Band Superconducting State for Lead Using Scanning Tunneling Spectroscopy, *Phys. Rev. Lett.* **114**, 157001 (2015).
- [87] J. R. Persson, Hyperfine structure and hyperfine anomaly in Pb, *J. Phys. Commun.* **2**, 055028 (2018).